Hypersonic Boundary-Layer Transition over a Blunt Circular Cone in a Mach 8 Digital Wind Tunnel

Mateus Schuabb* and Lian Duan†
The Ohio State University, Columbus, OH 43210, USA

Anton Scholten‡
North Carolina State University, Raleigh, NC 27695, USA

Pedro Paredes§
National Institute of Aerospace, Hampton, VA 23666, USA

Meelan M. Choudhari¶
NASA Langley Research Center, Hampton, VA 23681, USA

To understand the effects of freestream acoustic disturbances on transition reversal over a blunt body, three-dimensional direct numerical simulations (DNS) were conducted to investigate the interaction of a tunnel-like acoustic disturbance field with a Mach 8 laminar boundary layer over a 7 deg half-angle blunt cone with a nose radius of $R_n = 5.2$ mm. The flow conditions and the axisymmetric cone geometry matched those measured in the Sandia Hypersonic Wind Tunnel at Mach 8 (Sandia HWT-8), and the incident freestream acoustic disturbances in the DNS were generated by acoustic radiation from the nozzle-wall turbulent boundary layer in the same tunnel. Consistent with the predictions of the nonmodal instability analysis, the study shows the emergence of a second spectral peak for moderately oblique waves between 150 kHz and 200 kHz in the aft part of the cone. The spectral energy of temperature and streamwise velocity fluctuations is initially concentrated within the entropy layer. These fluctiations are eventually "swallowed" by the boundary layer as the entropy-layer thickness δ_S becomes similar to the boundary-layer thickness δ_{ht} at downstream locations. The numerical schlieren contours show the same inclined structures commonly observed in blunt cone experiments, and these structures are found to be three dimensional and advect with a constant speed approximately equal to the mean flow speed near the edge of the boundary layer.

Nomenclature

C_f = skin friction coefficient, $C_f = \tau_w/(0.5\rho_\infty U_\infty^2)$, dimensionless
C_h = mean Stanton number,$C_h = q_w/(\rho_\infty U_\infty C_p(T_r - T_w))$, dimensionless
C_p = heat capacity at constant pressure, J/(K·kg)
C_v = heat capacity at constant volume, J/(K·kg)
E = total energy norm, J
f = frequency, Hz
H = shape factor, $H = \delta^*/\theta$, dimensionless
h_ξ = streamwise metric factor
h_ζ = spanwise metric factor, m
J = objective function
M = Mach number, dimensionless
m = azimuthal wavenumber, rad^{-1}

*Graduate Student, Department of Mechanical and Aerospace Engineering
†Associate Professor, Department of Mechanical and Aerospace Engineering, Associate Fellow, AIAA
‡Graduate Student, Department of Mechanical and Aerospace Engineering, Student Member, AIAA
§Associate Research Fellow, Computational AeroSciences Branch, NASA LaRC. Associate Fellow, AIAA
¶Aerospace Technologist, Computational AeroSciences Branch, M.S. 128. Fellow, AIAA

N = Logarithmic amplification factor
$\hat{\mathbf{q}}$ = vector of amplitude variables
$\breve{\mathbf{q}}$ = vector of disturbance function variables
$\bar{\mathbf{q}}$ = vector of base flow variables
$\tilde{\mathbf{q}}$ = vector of perturbation variables
Pr = Prandtl number, $Pr = 0.71$, dimensionless
R = ideal gas constant, $R = 287$, J/(K·kg)
Re_∞ = freestream unit Reynolds number, $Re_\infty = \frac{\rho_\infty U_\infty}{\mu_\infty}$, m^{-1}
Re_θ = Reynolds number based on momentum thickness and freestream viscosity, $Re_\theta \equiv \frac{\rho_\infty U_\infty \theta}{\mu_\infty}$, dimensionless
Re_{δ_2} = Reynolds number based on momentum thickness and wall viscosity, $Re_{\delta_2} \equiv \frac{\rho_\infty U_\infty \theta}{\mu_w}$, dimensionless
Re_τ = Reynolds number based on shear velocity, boundary-layer thickness, and wall viscosity, $Re_\tau \equiv \frac{\rho_w u_\tau \delta}{\mu_w}$, dimensionless
S = entropy, $S = \frac{\gamma}{\gamma-1} \ln \frac{T}{T_\infty} - \ln \frac{p}{p_\infty}$, dimensionless
T = temperature, K
T_r = recovery temperature, $T_r = T_\infty(1 + 0.9 * \frac{\gamma-1}{2} M_\infty^2)$, K
U_∞ = freestream velocity, m/s
a = speed of sound, m/s
p = pressure, Pa
q = dynamic pressure, Pa
r = radial coordinate
u = streamwise velocity, m/s
u_τ = friction velocity, $u_\tau \equiv \tau_w / \overline{\rho}_w$, m/s
v = spanwise velocity, m/s
w = wall-normal velocity, m/s
x = streamwise direction of the right hand Cartesian coordinate
y = spanwise direction of the right hand Cartesian coordinate
z = wall-normal direction of the right hand Cartesian coordinate
z_τ = viscous length, $z_\tau = \nu_w / u_\tau$, m
γ = specific heat ratio, $\gamma = C_p / C_v$, dimensionless
δ = boundary layer thickness (based on 99.5% of the total enthalpy), m
δ^* = displacement thickness, m
δ_S = entropy layer thickness at $S/S_{wall} = 0.25$, m
δ_{ht} = boundary layer thickness based on the maximum of the total enthalpy, m
δ_M = wall-normal location of the sonic line $M = 1$, m
κ = thermal conductivity, $\kappa = \mu C_p / Pr$, W/(m·K)
θ = momentum thickness, m
μ = dynamic viscosity, kg/(m·s)
ν = kinematic viscosity, $\nu = \mu / \rho$, m^2·s
ρ = density, kg/m^3
τ_w = wall shear stress, Pa

Subscripts

e = boundary-layer edge variables
i = inflow station for the domain of direct numerical simulations
o = stagnation quantities
rms = root mean square
w = wall variables
∞ = freestream variables

Superscripts

$+$ = inner wall units
$\overline{(\cdot)}$ = statistically averaged variables
$(\cdot)'$ = perturbation from averaged variable

I. Introduction

Boundary layer transition (BLT) accounts for a major source of uncertainty in the heating loads on high-speed vehicles. Therefore, the prediction and control of transition onset and the associated variation in aerothermodynamic parameters in high-speed flows are critical factors in the design of next-generation aerospace vehicles. While many practical high-speed vehicles are blunt, the mechanisms that lead to boundary layer instability and transition on blunt bodies are much less thoroughly understood at present compared to those on sharp bodies. Particularly elusive have been the role played by the entropy layer in the nose region of a blunted cone and the phenomenon of "transition reversal" [1]. While experiments in conventional (i.e., "noisy") hypersonic wind tunnels indicate that the delay in boundary-layer transition at a small nose bluntness eventually slows down and reverses as the nose bluntness exceeds a certain critical range of values [1–6], the linear modal stability theory predicts a continual delay in transition onset without reversal at large nose bluntness. Alternative theoretical paradigms based on nonmodal disturbance amplification have been proposed to explain the phenomenon of transition reversal [7–10]. However, the scope of the nonmodal analyses did not extend to addressing the origin of these nonmodal traveling disturbances that peak within the entropy layer. A follow-on study is therefore necessary to provide further information regarding the role of the freestream disturbances and the nonmodal growth of traveling disturbances within the entropy layer during the transition process. It is particularly important to establish a link between measured transition in the absence of modal disturbance amplification and the freestream acoustic disturbances in a noisy wind-tunnel environment, given that almost all available experimental observations of the blunt cone transition phenomenon have been made in conventional hypersonic wind tunnels.

Complementary to experiments and theories, high-fidelity direct numerical simulations (DNS) have been performed to study the instability process in the entropy layer in the nose region of blunted cones at hypersonic Mach numbers. To date, most DNS of hypersonic blunt cones have been carried out using either controlled forcing at the inlet or within the domain with a broadband of frequencies and wave numbers [11–14] or assumed incoming freestream disturbance fields with plane acoustic waves [15, 16]. For study of receptivity to freestream acoustic disturbances in particular, Balakumar and Chou [16] conducted hypersonic boundary-layer flows over a 7° half-angle straight cone with varying bluntness at a freestream Mach number of 10. In their study, an attempt was made to predict transition onset for flow over cones by using measured freestream spectrum and two-dimensional numerical simulations. Only plane two-dimensional acoustic waves were imposed in the simulations, unlike the noise radiated from the nozzle walls that impinges on a test article at oblique angles. Although this approach provided encouraging results for a sharp cone under different flow conditions, the predictions for the flow over a medium blunt cone were not very satisfactory. Balakumar et al. [17] further examined the response of a Mach 3.5 flow over a sharp 7° half-angle cone to oblique acoustic waves described by ad hoc analytical expressions. However, it is unclear how well this simple form of freestream disturbances would perform in predicting BLT over a blunt body.

To elucidate the role of the freestream disturbances and the nonmodal growth of traveling disturbances within the entropy layer during the transition process, Liu et al. [18] performed DNS and nonmodal stability analysis to study boundary-layer receptivity to broadband freestream acoustic disturbances from the nozzle wall of a digital conventional wind tunnel at Mach 8. In their DNS, a "tunnel-like" acoustic disturbance field, that reproduces both the frequency-wavenumber spectra and the temporal evolution of the broadband tunnel noise radiated from the nozzle wall, was input above the bow shock of a 7-degree half-angle cone with a nose radius of $R_n = 5.2$ mm. The DNS showed prominent entropy layer disturbances resembling the predictions of nonmodal growth [10]. The DNS-predicted spectra of wall-pressure and heat-transfer fluctuations were shown to recover the signature of the axisymmetric waves predicted by the nonmodal analysis, and the numerical schlieren contours of the DNS showed similar inclined structures commonly observed in blunt cone experiments. The current paper extends the pioneering DNS of Liu et al. [18] by including a longer length of the cone, along with more detailed data analysis to provide further information regarding the downstream evolution of the prominent entropy layer disturbances. The goal is to characterize tunnel-noise effects within the transition reversal regime, by helping to establish a more definitive link between the nonmodal growth of disturbances and the observed onset of transition in the absence of substantial modal disturbance growth.

The paper is structured as follows. The flow conditions and numerical methods are outlined in Section II. Section III presents DNS results for studying the interaction of a tunnel-like acoustic disturbance field with a 7° half-angle blunt cone with nose radius of 5.20 mm at Mach 8. A summary of the planned work is given in Section IV.

II. Flow Conditions and DNS Methodology

DNS of boundary-layer instability and transition are conducted over a 0.517-meter-long, 7° half-angle cone with a blunt nose radius of 5.2 mm. To simulate BLT over the cone model within a digital wind tunnel, a precursor DNS of the

Table 1 Preshock freestream conditions and wall temperature for DNS of a Mach 8 cone.

$M_{1,\infty}$	$U_{1,\infty}$(m/s)	$\rho_{1,\infty}$ (kg/m^3)	$T_{1,\infty}$ (K)	T_w (K)	T_w/T_r	$Re_\infty \times 10^6$ (1/m)
8.085	1091.82	0.0345	43.90	298	0.537	12.2

full-scale axisymmetric nozzle of the Sandia HWT-8 was first conducted at a nominal operational condition of total pressure of $P_0 \approx 4692$ kPa and total temperature of $T_0 \approx 617$ K, and the flow conditions (including the unsteady acoustic disturbances) at the center of the nozzle near the nozzle exit were extracted and used for the primary cone simulation. More details of the precursor DNS of the digital wind tunnel along with the methodology for extracting freestream acoustic disturbances was described in Liu et al. [18]. Table 1 summarizes the extracted mean freestream conditions used for the current cone DNS. The wall temperature of the cone is 298 K, corresponding to a wall-to-recovery temperature ratio of $T_w/T_r \approx 0.537$.

To simulate boundary-layer instability and transition on a circular cone, the full three-dimensional compressible Navier-Stokes equations in conservation form were solved numerically in cylindrical coordinates. The working fluid was nitrogen (with an ideal gas constant of $R = 296.7$ J/(K·kg)) and fell within the perfect gas regime. The usual constitutive relations for a Newtonian fluid were used: the viscous stress tensor was linearly related to the rate-of-strain tensor, and the heat flux vector was linearly related to the temperature gradient through Fourier's law. The coefficient of molecular viscosity μ was computed from Keyes law [19], and of thermal conductivity, κ, was computed from $\kappa = \mu C_p/Pr$, with the molecular Prandtl number, $Pr = 0.71$. The inviscid fluxes of the governing equations were computed using a seventh-order weighted essentially nonoscillatory (WENO) scheme [20]. The viscous fluxes were discretized using a fourth-order central difference scheme, and time integration was performed using a third-order low-storage Runge-Kutta scheme [21]. The singularity at the polar axis, as manifested in the $1/r$ terms of the governing equations, is handled by shifting the grid points in the radial direction by one-half of the mesh spacing, following the approach proposed by Mohseni and Colonius [22]. In their approach, the use of less accurate one-sided finite difference schemes for the purpose of evaluating radial derivatives close to the pole ($r = 0$) is eliminated by mapping the flow domain from $(0, R) \times (0, 2\pi)$ to $(-R, R) \times (0, \pi)$, where R is the radius of the computational domain. The time step limitation due to the decrease in azimuthal spacing in the vicinity of the centerline (or pole) is addressed by dropping every few grid points (which amounts to increasing the grid spacing) in the azimuthal direction as $r \to 0$ in the computation of the azimuthal derivative [23]. The cone DNS has been conducted in multiple stages, and each stage computes the solutions for different streamwise domains, where each domain overlaps the adjacent ones. Thus, the time step can be larger for further the downstream domains, and also, the number of points in the azimuthal direction can increase considering that the azimuthal length increases as x increases. A similar multidomain simulation approach of this type was previously applied to the DNS of BLT over a cone [24, 25]. Additional details of the DNS methodology have been documented in our previous paper [18].

To numerically investigate the transitional and turbulent boundary layer over a circular cone that is subject to "tunnel-like" freestream acoustic disturbances, the DNS is set up with the inflow boundary of the computational domain lying outside the leading-edge shock of the cone. "Tunnel-like" freestream acoustic disturbances are then introduced by prescribing flow variables at the inflow boundary based on the data saved from the precursor DNS of the disturbance environment inside a digital wind tunnel that pertains to an empty wind-tunnel configuration (i.e., without the test article). Fluctuation data within the freestream region of the precursor DNS are extracted and, after necessary reconstruction, fed through the outer boundary of the computational domain of the DNS involving the cone (See Liu et al. [18] for details of the tunnel-noise extraction process). On the wall, no-slip conditions are applied for the three velocity components, and an isothermal condition is used for the temperature. In the last 150 points in the axial direction in each box, the grid has been stretched to dampen acoustic reflections, and unsteady nonreflecting boundary conditions are imposed at the outlet boundaries. Periodic boundary conditions are used in the azimuthal direction, with an azimuthal domain that covers the 360 degrees of the geometry.

For the current work, considering the significant azimuthal meandering of the strongly curved shock near the nose region of the cone due to its interaction with the freestream acoustics waves, we have rerun part of the simulations with increased number of points in the azimuthal direction and with the introduction of an azimuthal spectral filter immediately behind the strongly curved portion of the shock at $x = 0.105$ m to remove any spurious two-point oscillations originating from the shock-capturing scheme due to the misalignment of the azimuthal grid line and the deformed shock. Figure 1 shows the DNS setup used in our updated work, wherein the streamwise location of the azimuthal

spectral filter corresponds to the intersection of Box 2 and Box2b. The details of the grid dimensions, domain size, and resolutions for each DNS boxes are listed Table 2. N_x, N_θ and N_r are the grid points in the streamwise, azimuthal, and radial directions, respectively. The range of x indicates the streamwise domain range of each DNS boxes. Δx^+ is the streamwise wall-paralleled grid spacing, $(r\Delta\theta)^+$ is the azimuthal grid spacing at the wall, and $\Delta z_{n,w}$ and $\Delta z_{n,e}$ are the wall-normal grid spacing at wall and boundary-layer edge, respectively. The leading edge of the cone corresponds to $x = -5.2$ mm, and the superscript "+" denotes normalization by the viscous length z_τ at $x = 0.3$ m for all the boxes. The numerical noise due to shock oscillations is confirmed to be negligibly small in comparison to the input tunnel noise disturbances after the filtering is applied, which allows to establish a more definitive link between tunnel noise and the nonmodal growth of disturbances.

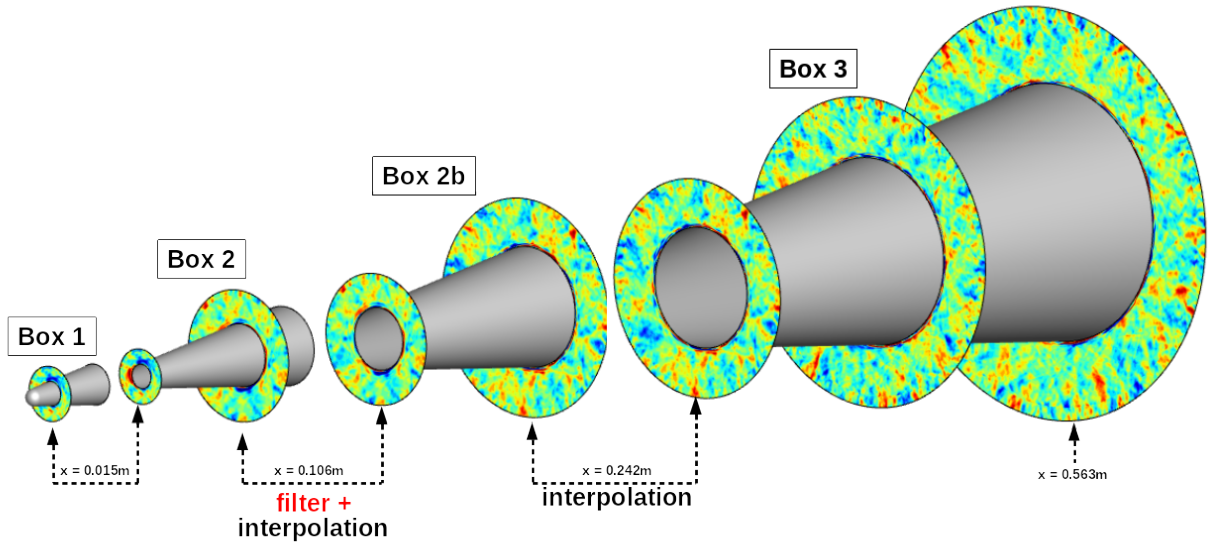

Fig. 1 Computational domain and simulation setup for the updated DNS of Mach 8 flow over a blunt 7-deg half-angle circular cone with a blunt nose radius of $R_n = 5.2$ mm.

Table 2 Domain size and grid resolution for the cone DNS runs.

Case	$N_x \times N_\theta \times N_r$	t (ms)	x (m)	Δx^+_{min}	Δx^+_{max}	$(r\Delta\theta)^+_{min}$	$(r\Delta\theta)^+_{max}$	$\Delta z^+_{n,w}$
Box 1	$2800 \times 256 \times 1440$	[0.0, 0.58]	[-0.0061 - 0.02]	0.23	0.23	0.003	4.28	0.11
Box 2	$1050 \times 256 \times 1440$	[0.01,0.58]	[0.015 - 0.144]	0.23	4.72	4.18	13.46	0.27
Box 2b	$900 \times 512 \times 1440$	[0.08,0.58]	[0.106 - 0.252]	4.72	4.72	5.34	10.58	0.34
Box 3	$1800 \times 1024 \times 1440$	[0.21,0.58]	[0.242 - 0.563]	4.72	4.72	5.12	10.89	0.54

III. Results

The results of the three-dimensional DNS of a Mach 8 blunt cone with $R_n = 5.2$ mm are discussed next. In our previous work by Liu et al. [18], we ran the solution until ≈ 0.48 milliseconds (ms), representing approximately 0.95 flow through time. However, in this paper, we have extended this time to 0.58 ms, which represents around 1.15 flow through time, an increase of 20% in run time, and, consequently, more statistically converged results. As a reference for the following results, the leading edge of the cone corresponds to $x = -5.2$ mm. As explained in Section II, the reconstructed, tunnel-like freestream acoustic disturbances described in Liu et al. [18] are used as the inflow forcing along the freestream boundary of the computational grid upstream of the bow shock. The full azimuthal domain of 2π radians is included in the DNS.

Figure 2 shows the comparison in the evolution of the mean skin-friction coefficient $C_f = \tau_w/(0.5\rho_{2,\infty}U^2_{2,\infty})$, the mean Stanton number $C_h = q_w/(\rho_{2,\infty}U_{2,\infty}C_p(T_r - T_w))$, and the mean wall pressure predicted by the current DNS

against those of Liu et al. [18]. No significant difference is seen between old and new simulations in these wall statistics. In both cases, the modeled freestream acoustic disturbances lead to Stanton number values that are approximately 10% higher in the nosetip region, and at approximately $x \approx 0.08$ m, there is a small difference smaller than 1% in the wall pressure between baseflow and the new DNS results. However, both the Stanton number and the wall pressure for the acoustic forcing case recover to the laminar baseflow values for $x > 0.15$ m. The skin-friction coefficient for both cases is very similar to the baseflow values and there is no sign of an increase in the skin-friction or heat transfer coefficient, indicating that the flow remains laminar at least up to $x = 0.55$ m.

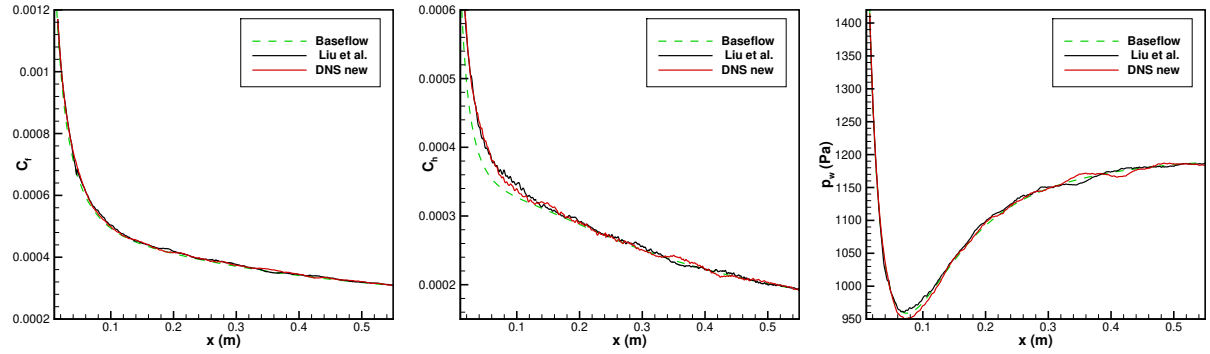

(a) (b) (c)

Fig. 2 (a) Skin-friction coefficient, (b) Stanton number, and (c) wall pressure over the Mach 8 cone of $R_n = 5.2$ mm predicted by the current DNS and that of Liu et al. [18].

The linear disturbances can be considered harmonic in time and azimuthal direction so that they can be decomposed into Fourier modes. Then, the following spectral results are Fourier transformed in time and/or the azimuthal coordinate. Figure 3 shows the DNS-predicted spectral amplitude of the fluctuations in wall pressure, surface heat flux, and wall skin-friction in the frequency (f) and azimuthal wavenumber (m) plane, where m can be computed by $m = 2\pi/\lambda_\theta$ being λ_θ is the azimuthal wavelength. At the upstream locations, the highest values of spectral density for all the wall quantities are mostly confined to the low frequency range of up to approximately 50 kHz. Such a range coincides with a major fraction of the signal energy in the tunnel-like freestream acoustic disturbances as reported in Liu et al. [18]. In the aft part of the cone, however, a secondary peak emerges at higher frequencies in the range of 150 kHz to 200 kHz and azimuthal wavenumbers lower than approximately 40. The emergence of a secondary peak in the same range of frequencies and for small values of m is also predicted by the optimal growth analysis shown in Liu et al. [18]. This secondary peak is further visualized in Figure 4, which plots the frequency spectrum as a function of the streamwise coordinate x. For all the wall quantities, the appearance of a second peak between 150 kHz to 200 kHz is apparent at $x \approx 0.20$ m, and the peak persists over the entire streamwise domain with nearly a constant magnitude. No superharmonics of the peak has yet appeared within the computational domain.

Next, we analyze the wall-normal variation of the disturbance spectra at multiple different streamwise locations. Figures 5 and 6 show the azimuthal wavenumber and frequency spectra of pressure p', temperature T', and streamwise velocity u' fluctuations. In each figure, δ_S, δ_{ht}, and δ_M represents the entropy layer thickness at $S/S_{wall} = 0.25$, the boundary layer thickness based on the maximum of the total enthalpy, and the wall-normal location of the sonic line for the baseflow, respectively. From the pressure results, at all streamwise locations, we can see that the boundary layer acts as a low-pass filter, i.e., only disturbances with small frequencies and small azimuthal wavenumbers penetrate into the boundary layer. Moreover, the same secondary peak around $f \approx 175$ kHz in the near wall region seen in the previous plots can also be observed. At $x \approx 0.2$ m, this peak starts appearing, and it becomes more evident in more downstream locations. In addition, it can be seen that it is located at the wall, and confined below the sonic line. Furthermore, from the frequency spectra of temperature fluctuation in Figure 6, it is also possible to observe this secondary peak around $f \approx 175$ kHz, and also confined between the wall and the sonic line. However, its maximum is not at the wall since we considered an isothermal wall along the entire cone surface. Previous work [9] suggests that this peak is related to the nonmodal entropy layer instability. Additionally, the frequency spectrum is more broad close to the entropy layer edge, while the azimuthal wavenumber spectrum is more broad between the boundary-layer edge and the sonic line. Finally, one of the most important observations is that the additional peak around $m \approx 128$ seen in the previous DNS of

Liu et al. [18] no longer exists after the filtering at an upstream location, confirming that the peak was indeed due to numerical noise. In these new results, most of the energy spectra are concentrated for small azimuthal wavenumber. In both spectra for the streamwise velocity fluctuation, most of the signal energy is inside the boundary layer for the selected locations. It may be observed that the wavenumber spectra become more broad at further downstream location, while the frequency spectra remain nearly unchanged.

Figure 7 shows the fluctuation magnitude associated with a given frequency and azimuthal wavenumber of (f, m) = (177.8 kHz, 0) at three different streamwise locations. The temperature disturbance is shown to peak very close to the edge of the entropy layer (δ_S), while the peak of the pressure disturbance typically lies above the entropy layer. In addition to the outer peak within the entropy layer, a near-wall peak below the sonic line is also apparent in both temperature and pressure disturbances, with peak amplitude remaining constant across the streamwise domain.

Figure 8 shows the temporal/spatial evolution of the numerical schlieren contours in the x-r plane. Similar to experimental observations in conventional wind tunnels for blunt straight cones [26, 27] or blunt ogive-cylinder [28], one observes the appearance of inclined structures that extend above the boundary-layer edge. Since these inclined structures do not appear for sharp cones [27], and in the baseflow without freestream acoustics disturbances, we can suggest that such structures are likely to be excited by freestream acoustic disturbances in the presence of an entropy layer due to the blunt nosetip. Figure 8 further tracks the time evolution of a typical inclined structure. The structure is shown to advect with a constant speed without much variations in size or shape, and the convection speed of this structure is found to be approximately equal to the mean flow speed near the edge of the boundary layer. A similar observation was made by Kennedy et al. [27] in their experimental study for a blunt cone in a conventional Mach 6 Ludwieg tube. It is worth mentioning that the inclined structures are very similar to those observed in Liu et al. [18], indicating that the current applications of an azimuthal filter in the current work at an upstream location has negligible impact on the excitation of downstream flow structures.

Finally, Figure 9 plots an isosurface of the numerical schlieren colored by the local wall-normal distance to provide a three-dimensional view of typical inclined structures as shown in Figure 8. A zoomed-in three-dimensional view of such structures is further given in Figure 10. The inclined structures are indeed three-dimensional, initially residing outside of the boundary layer but becoming closer the the wall as they advect downstream. However, the three dimensional structures are free of the spurious periodic azimuthal patterns as observed in the old simulations of Liu et al. [18], which were presumably caused by numerical noise and have been successfully removed by the upstream azimuthal filter.

IV. Summary

The interaction of a tunnel-like acoustic disturbance field with a Mach 8 laminar boundary layer over a 7 deg half-angle blunt cone with a nose radius of R_n = 5.2 mm has been investigated by using DNS. The imposed freestream disturbances in the DNS are planar acoustic waves modeled based on a digital wind tunnel to mimic the acoustic radiation from turbulent boundary layers on the walls of a Mach 8 conventional wind tunnel. As a continuation of our previous work by Liu et al. [18], we investigated the origin of the prominent three-dimensional disturbances in the entropy layer by including a longer length of the cone, along with more detailed data analysis.

The study shows that, while most of the signal energy at the wall is confined to small frequencies and small wavenumbers, there exists an additional concentration of energy for moderately oblique waves between frequencies 150 kHz and 200 kHz in the aft part of the cone, which agrees well with the predictions of the nonmodal instability analysis. The emergence of such a secondary peak occurs at $x \approx 0.2$ m, and its amplitude remains nearly constant along the cone length. The temperature fluctuations frequency spectra show a very broadband signal with frequencies up to 300 kHz around the entropy layer edge. These fluctuations are associated with lower azimuthal wavenumbers than the fluctuations that evolve within the boundary layer. The streamwise fluctuations are contained within the entropy layer and peak inside the boundary layer. As the entropy layer is swallowed by the boundary layer when their thicknesses become comparable, a broader spectra of the fluctuations are observed within the boundary layer. The numerical schlieren contours show the same inclined structures commonly observed in blunt cone experiments. These structures correspond to three-dimensional structures that advect with a constant speed equal to the mean flow speed near the edge of the boundary layer.

Notably, the azimuthal wavenumber spectrum of temperature fluctuations is free of a spectral peak at $m \approx 128$ as shown in the previous DNS by Liu et al. [18]. Consistently, the three-dimensional structures are free of the spurious periodic azimuthal patterns shown before. Such a spurious spectral peak and the periodic azimuthal patterns were presumably caused by numerical noise and are shown to be successfully removed by applying an azimuthal filter in an upstream plane.

Future work will include DNS runs for longer periods of time and locations further downstream of the cone to capture the final breakdown stages of the laminar-turbulent transition. Such additional simulations will provide further information regarding the role of the freestream disturbances and the nonmodal growth of traveling disturbances within the entropy layer during the transition process.

Acknowledgments

This work by Mateus Schuabb and Lian Duan relates to Department of Navy award N00014-23-1-2456 issued by the Office of Naval Research under a subaward from the National Institute of Aerospace. Anton Scholten was supported by the ONR under grant N00014-20-1-2261, managed by Dr. Eric Marineau. Pedro Paredes was partially supported by the ONR under grants N00014-20-1-2261 and N00014-23-1-2456, managed by Dr. Eric Marineau, and by the Hypersonic Technology Project (HTP) under the NASA Aeronautics Research Mission Directorate (ARMD). Meelan Choudhari was supported by the HTP under the NASA ARMD. Computational resources were provided by the DoD High-Performance Computing Modernization Program and the Ohio Supercomputer Center. Any opinions, findings, and conclusions or recommendations expressed in this material are those of the author(s) and do not necessarily reflect the views of the National Institute of Aerospace, the Office of Naval Research, or the U.S. Government.

References

[1] Stetson, K., "Nosetip Bluntness Effects on Cone Frustum Boundary Layer Transition in Hypersonic Flow," *AIAA Paper 1983-1763*, 1983. https://doi.org/10.2514/6.1983-1763.

[2] Marineau, E. C., Moraru, C. G., Lewis, D. R., Norris, J. D., Lafferty, J. F., Wagnild, R. M., and Smith, J. A., "Mach 10 Boundary-Layer Transition Experiments on Sharp and Blunted Cones," *AIAA Paper 2014-3108*, 2014. https://doi.org/10.2514/6.2014-3108.

[3] Jewell, J. S., and Kimmel, R. L., "Boundary-Layer Stability Analysis for Stetson'sMach6 Blunt-Cone Experiments," *Journal of Spacecraft and Rockets*, Vol. 54, No. 1, 2017, pp. 258–265. https://doi.org/10.2514/1.A33619.

[4] Jewell, J. S., Kennedy, R. E., Laurence, S. J., and Kimmel, R. L., "Transition on a Variable Bluntness 7-Degree Cone at High Reynolds Number," *AIAA Paper 2018-1822*, 2018. https://doi.org/10.2514/6.2018-1822.

[5] Paredes, P., Choudhari, M. M., Li, F., Jewell, J. S., Kimmel, R. L., Marineau, E. C., and Grossir, G., "Nosetip Bluntness Effects on Transition at Hypersonic Speeds: Experimental and Numerical Analysis Under NATO STO AVT-240," *AIAA Paper 2018-0057*, 2018. https://doi.org/10.2514/6.2018-0057.

[6] Kennedy, R. E., Jewell, J. S., Paredes, P., and Laurence, S. J., "Characterization of Instability Mechanisms on Sharp and Blunt Slender Cones at Mach 6," *Journal of Fluid Mechanics*, Vol. 936, 2022, p. A39. https://doi.org/10.1017/jfm.2022.39.

[7] Cook, D. A., Thome, J., Brock, J. M., Nichols, J. W., and Candler, G. V., "Understanding Effects of Nose-Cone Bluntness on Hypersonic Boundary Layer Transition using Input-Output Analysis," *AIAA Paper 2018-0378*, 2018. https://doi.org/10.2514/6.2018-0378.

[8] Paredes, P., Choudhari, M. M., Li, F., Jewell, J. S., Kimmel, R. L., Marineau, E. C., and Grossir, G., "Nose-Tip Bluntness Effects on Transition at Hypersonic Speeds," *Journal of Spacecraft and Rockets*, Vol. 56, No. 2, 2019, pp. 369–387. https://doi.org/10.2514/1.A34277.

[9] Paredes, P., Choudhari, M. M., Li, F., Jewell, J. S., and Kimmel, R. L., "Nonmodal Growth of Traveling Waves on Blunt Cones at Hypersonic Speeds," *AIAA Journal*, Vol. 57, No. 11, 2019, pp. 4738–4749. https://doi.org/10.2514/1.J058290.

[10] Paredes, P., Choudhari, M., and Li, F., "Mechanism for Frustum Tranistion over Blunt Cones at Hypersonic Speeds," *Journal of Fluid Mechanics*, Vol. 894, 2020, p. A22. https://doi.org/10.1017/jfm.2020.261.

[11] Goparaju, H., Unnikrishnan, S., and Gaitonde, D. V., "Effects of Nose Bluntness on Hypersonic Boundary-Layer Receptivity and Stability," *Journal of Spacecraft and Rockets*, 2021, pp. 1–17. https://doi.org/10.2514/1.A34829.

[12] Hader, C., and Fasel, H. F., "Towards Simulating Natural Transition in Hypersonic Boundary Layers via Random Inflow Disturbances," *Journal of Fluid Mechanics*, Vol. 847, 2018. https://doi.org/10.1017/jfm.2018.386.

[13] Ran, W., Zare, A., Hack, M. P., and Jovanović, M. R., "Stochastic Receptivity Analysis of Boundary Layer Flow," *Physical Review Fluids*, Vol. 4, No. 9, 2019, p. 093901. https://doi.org/10.1103/PhysRevFluids.4.093901.

[14] Hartman, A. B., Hader, C., and Fasel, H. F., "Nonlinear Transition Mechanism on a Blunt Cone at Mach 6: Oblique Breakdown," *Journal of Fluid Mechanics*, Vol. 915, 2021, p. R2. https://doi.org/10.1017/jfm.2021.109.

[15] Zhong, X., and Ma, Y., "Boundary-Layer Receptivity of Mach 7.99 Flow over a Blunt Cone to Free-Stream Acoustic Waves," *Journal of Fluid Mechanics*, Vol. 556, 2006, p. 55. https://doi.org/10.1017/S0022112006009293.

[16] Balakumar, P., and Chou, A., "Transition Prediction in Hypersonic Boundary Layers using Receptivity and Freestream Spectra," *AIAA Journal*, Vol. 56, No. 1, 2018, pp. 193–208. https://doi.org/10.2514/1.J056040.

[17] Balakumar, P., King, R. A., Chou, A., Owens, L. R., and Kegerise, M. A., "Receptivity and Forced Response to Acoustic Disturbances in High-Speed Boundary Layers," *AIAA Journal*, Vol. 56, No. 2, 2018, pp. 510–523. https://doi.org/10.2514/1.J056145.

[18] Liu, Y., Schuabb, M., Duan, L., Paredes, P., and Choudhari, M., "Interaction of a Tunnel-Like Acoustic Disturbance Field With a Blunt Cone Boundary Layer at Mach 8," AIAA 2022-3250, 2022. https://doi.org/10.2514/6.2022-3250.

[19] Keyes, F. G., "A Summary of Viscosity and Heat-Conduction Data for HE, A, H_2, O_2, CO, CO_2, H_2O, and Air," *Transactions of the American Society of Mechanical Engineers*, Vol. 73, 1951, pp. 589–596. https://doi.org/10.1115/1.4016339.

[20] Jiang, G. S., and Shu, C. W., "Efficient Implementation of Weighted ENO Schemes," *Journal of Computational Physics*, Vol. 126, No. 1, 1996, pp. 202–228. https://doi.org/10.1006/jcph.1996.0130.

[21] Williamson, J., "Low-Storage Runge-Kutta Schemes," *Journal of Computational Physics*, Vol. 35, No. 1, 1980, pp. 48–56. https://doi.org/10.1016/0021-9991(80)90033-9.

[22] Mohseni, K., and Colonius, T., "Numerical Treatment of Polar Coordinate Singularities," *Journal of Computational Physics*, Vol. 157, 2000, pp. 787–795. https://doi.org/10.1006/jcph.1999.6382.

[23] Bogey, C., de Cacqueray, N., and Bailly, C., "Finite Differences for Coarse Azimuthal Discretization and for Reduction of Effective Resolution Near Origin of Cylindrical Flow Equations," *Journal of Computational Physics*, Vol. 230, 2011, pp. 1134–1146. https://doi.org/10.1016/j.jcp.2010.10.031.

[24] Balakumar, P., and Kegerise, M. A., "Receptivity of Hypersonic Boundary Layer over Straight and Flared Cones," *AIAA Journal*, Vol. 53, No. 8, 2015, pp. 2097–2109. https://doi.org/10.2514/1.J053432.

[25] Balakumar, P., and Chou, A., "Transition Prediction in Hypersonic Boundary Layers using Receptivity and Freestream Spectra," *AIAA Paper 2016-0847*, 2016. https://doi.org/10.2514/6.2016-0847.

[26] Grossir, G., Pinna, F., and Chazot, O., "Influence of Nose-Tip Bluntness on Conical Boundary-Layer Instabilities at Mach10," *AIAA Journal*, Vol. 57, No. 9, 2019, pp. 3859–3873. https://doi.org/10.2514/1.J057822.

[27] Kennedy, R., Jewell, J., Paredes, P., and Laurence, S., "Characterization of Instability Mechanisms on Sharp and Blunt Slender Cones at Mach6," *Journal of Fluid Mechanics*, Vol. 936, 2022, p. A39. https://doi.org/10.1017/jfm.2022.39.

[28] Hill, J., Oddo, R. A., Komives, J. R., Reeder, M. F., Borg, M. P., and Jewell, J. S., "Experimental Measurements of Hypersonic Instabilities over Ogive-Cylinders at Mach 6," *AIAA Journal*, 2022, pp. 1–17. https://doi.org/10.2514/6.2021-0153.

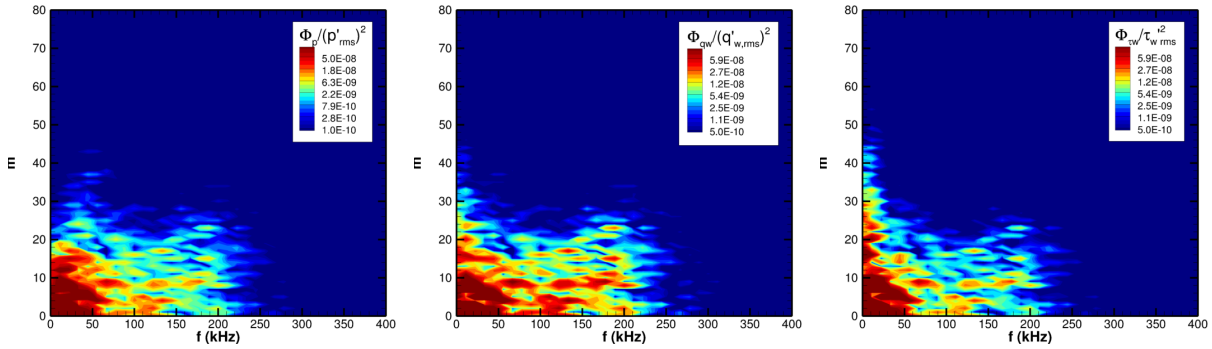

(a) $x = 0.20$ m

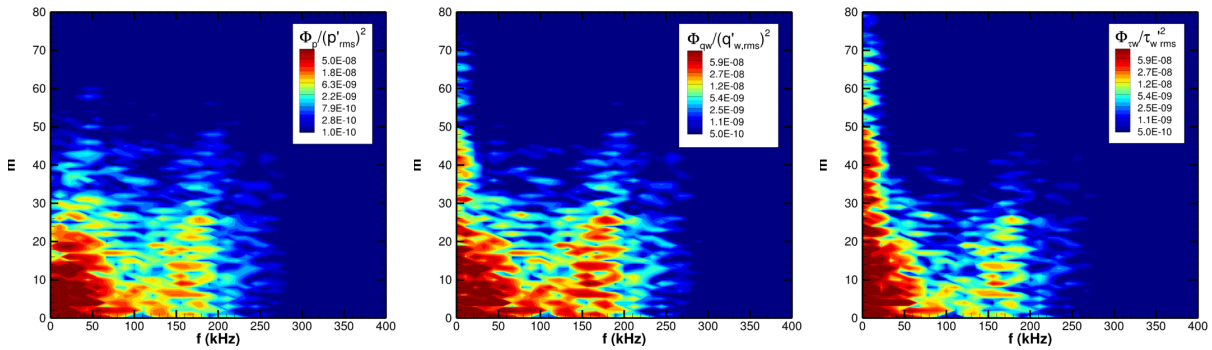

(b) $x = 0.30$ m

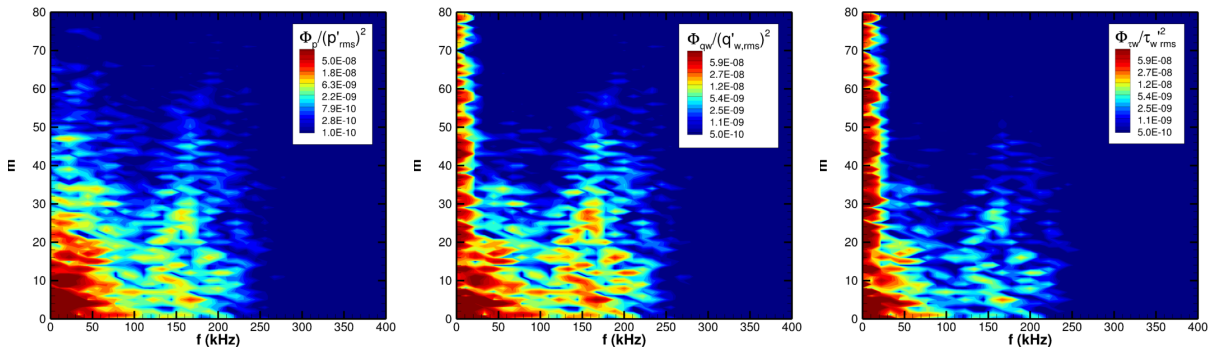

(c) $x = 0.40$ m

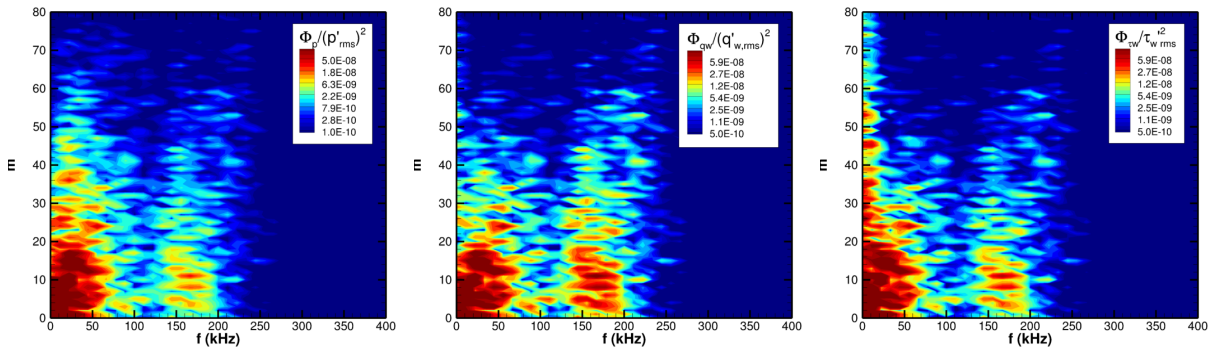

(d) $x = 0.50$ m

Fig. 3 Frequency/azimuthal-wavenumber ($f - m$) spectrum of the wall-pressure (first column), wall heat-flux (second column) and wall-skin-friction (third column) fluctuations over the Mach 8 cone of $R_n = 5.2$ mm predicted by three-dimensional DNS with tunnel-like acoustic input.

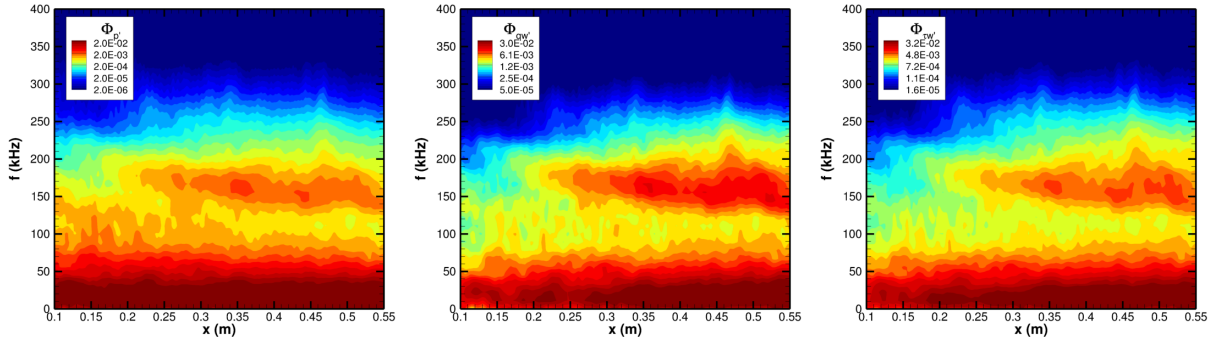

(a) Wall pressure, p_w (b) Wall heat-flux, q_w (c) Wall skin-friction, τ_w

Fig. 4 Normalized frequency spectrum of the wall-pressure, wall heat-flux, and wall skin-friction fluctuations as a function of the streamwise direction.

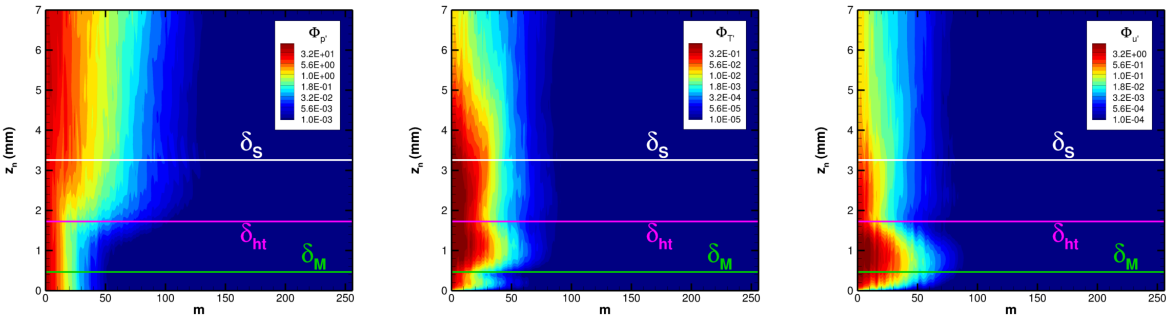

(a) x = 0.203 m

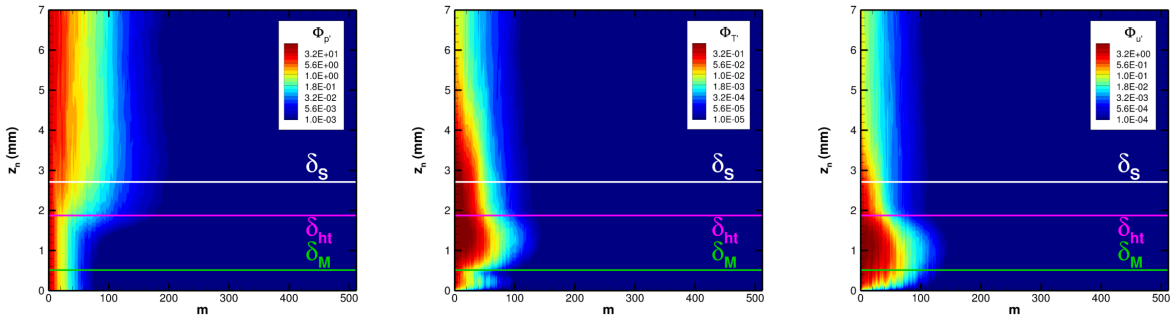

(b) x = 0.300 m

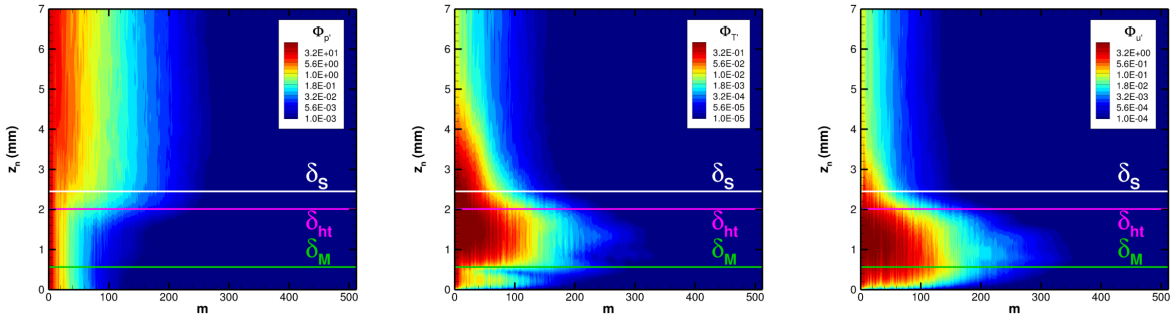

(c) x = 0.417 m

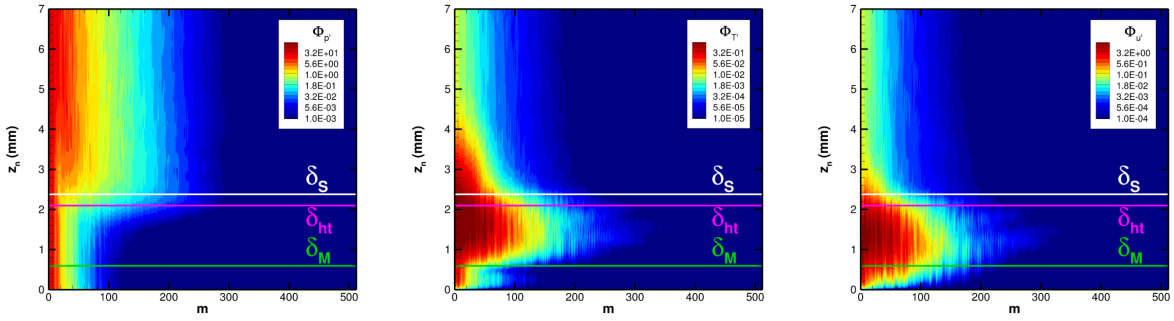

(d) x = 0.504 m

Fig. 5 Azimuthal wavenumber spectrum of pressure p' (first column), temperature T' (second column), and streamwise velocity u' (third column) fluctuations along a wall-normal profile at different streamwise locations.

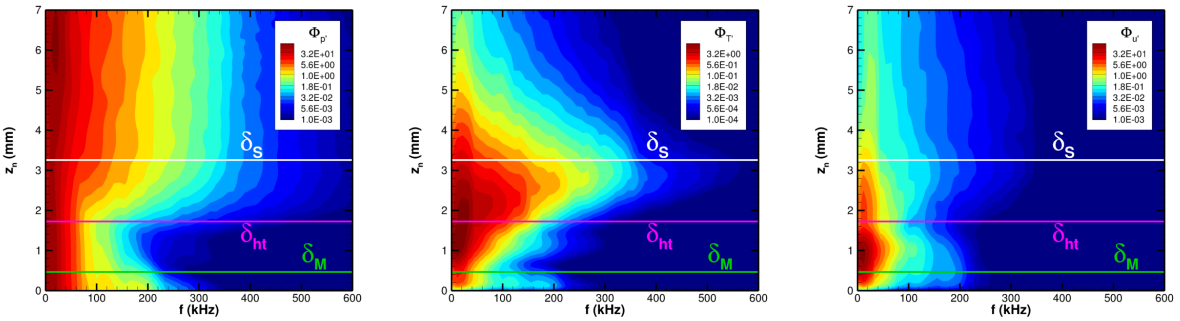

(a) x = 0.203 m

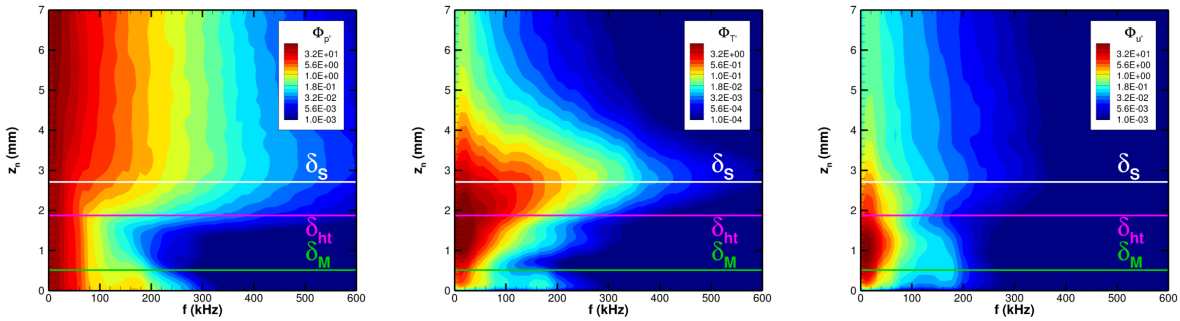

(b) x = 0.300 m

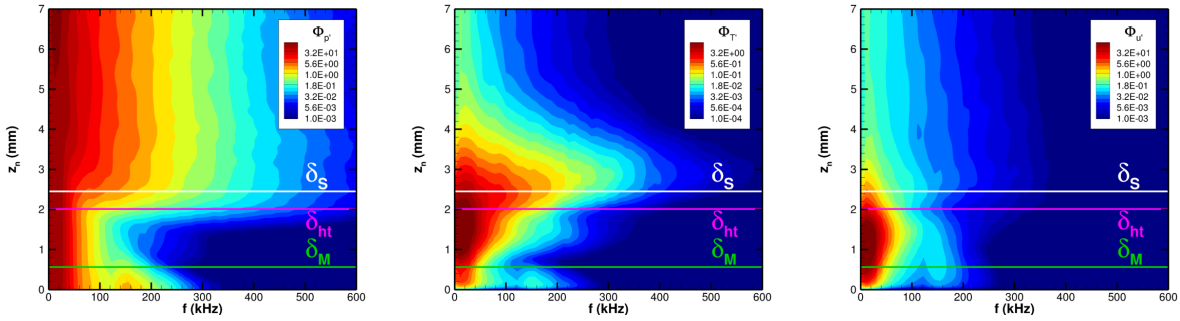

(c) x = 0.417 m

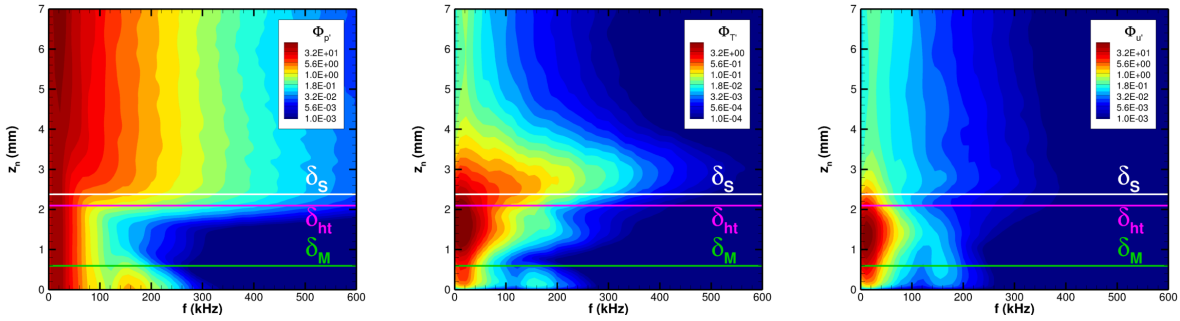

(d) x = 0.504 m

Fig. 6 Frequency spectrum of pressure p' (first column), temperature T' (second column), and streamwise velocity u' (third column) fluctuations along a wall-normal profile at different streamwise locations.

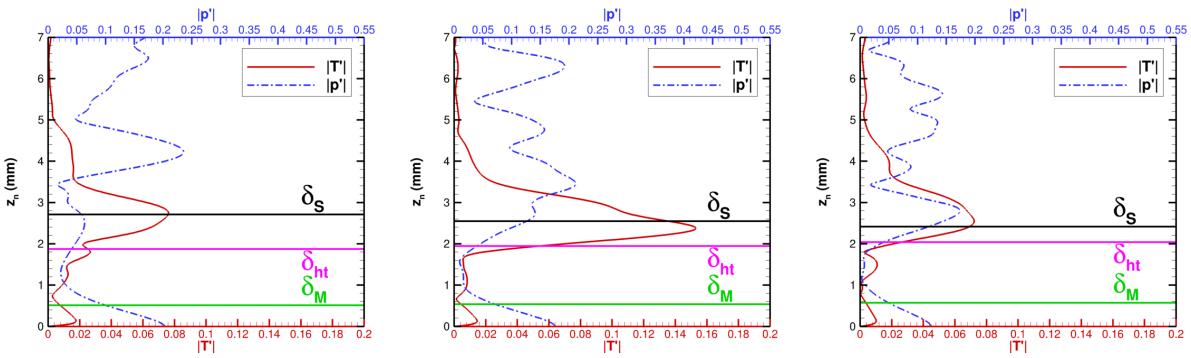

(a) $x \approx 0.300$ m (b) $x \approx 0.358$ m (c) $x \approx 0.446$ m

Fig. 7 Wall-normal distribution of pressure and temperature fluctuations for $(f - m)$ = (177.8 kHz, 0).

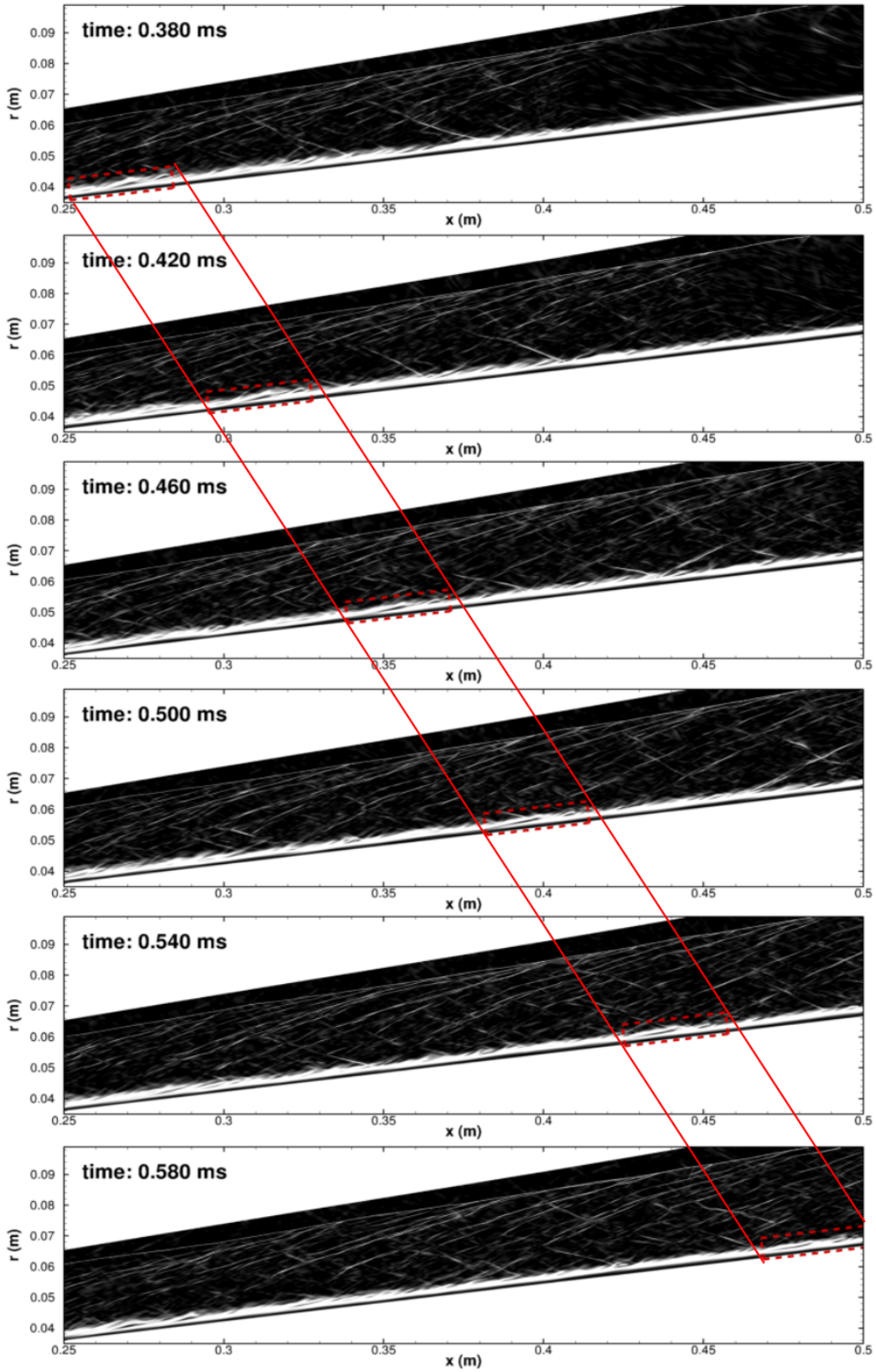

Fig. 8 Temporal/spatial visualization of the propagation of inclined structures that extend out of the boundary layer using numerical schlieren based on the density gradient.

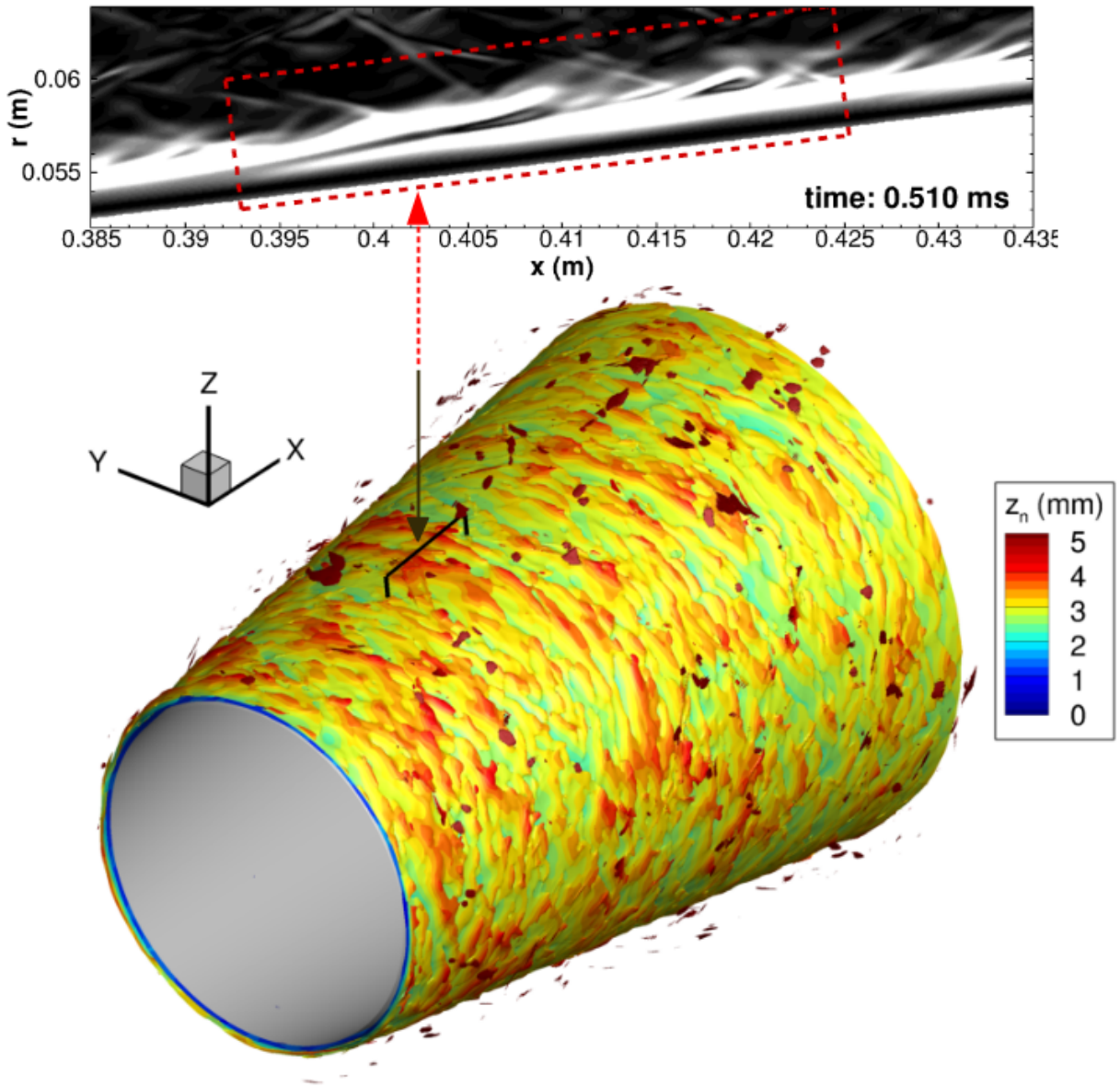

Fig. 9 Isosurface of the numerical schlieren (colored by the wall-normal distance z_n) over a cone section of x = [0.337,0.533] for the Mach 8 cone of $R_n = 5.2$ mm predicted by three-dimensional DNS with tunnel-like acoustic input.

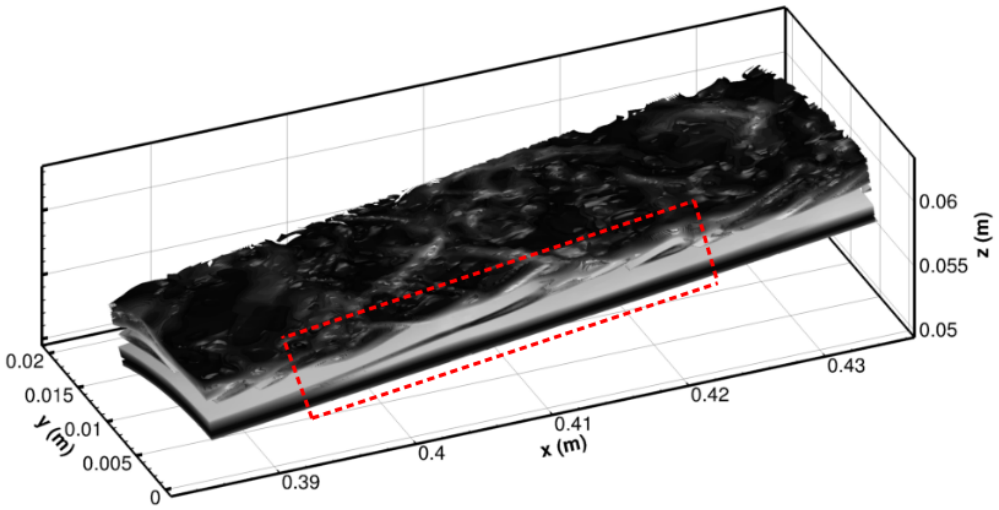

Fig. 10 Isosurface of the numerical schlieren over the entire cone for the Mach 8 cone of $R_n = 5.2$ mm predicted by three-dimensional DNS with tunnel-like acoustic input.